ACS NANO

www.acsnano.org

ARTICLE

Tracking the Effects of Ligands on Oxidative Etching of Gold Nanorods in Graphene Liquid Cell Electron Microscopy

Matthew R. Hauwiller, Xingchen Ye, Matthew R. Jones, Cindy M. Chan, Jason J. Calvin, Michelle F. Crook, Haimei Zheng, and A. Paul Alivisatos*

Cite This: *ACS Nano* 2020, 14, 10239–10250

Read Online

ACCESS | Metrics & More | Article Recommendations | Supporting Information

ABSTRACT: **Surface ligands impact the properties and chemistry of nanocrystals, but observing ligand binding locations and their effect on nanocrystal shape transformations is challenging. Using graphene liquid cell electron microscopy and the controllable, oxidative etching of gold nanocrystals, the effect of different ligands on nanocrystal etching can be tracked with nanometer spatial resolution. The chemical environment of liquids irradiated with high-energy electrons is complex and potentially harsh, yet it is possible to observe clear evidence for differential binding properties of specific ligands to the nanorods' surface. Exchanging CTAB ligands for PEG-alkanethiol ligands causes the nanorods to etch at a different, constant rate while still maintaining their aspect ratio. Adding cysteine ligands that bind preferentially to nanorod tips induces etching predominantly on the sides of the rods. This etching at the sides leads to Rayleigh instabilities and eventually breaks apart the nanorod into two separate nanoparticles. The shape transformation is controlled by the interplay between atom removal and diffusion of surface atoms and ligands. These *in situ* observations are confirmed with *ex situ* colloidal etching reactions of gold nanorods in solution. The ability to monitor the effect of ligands on nanocrystal shape transformations will enable future *in situ* studies of nanocrystals surfaces and ligand binding positions.**

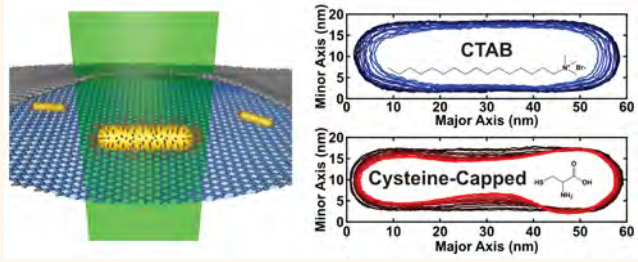

KEYWORDS: *transmission electron microscopy, gold nanocrystals, liquid cell, ligands, oxidative etching*

Colloidal nanocrystals exhibit emergent properties due to their small size, and these characteristics have been harnessed for a variety of optical,[1] catalytic,[2−5] biomedical,[6−8] energetic,[9,10] and other applications. For colloidal nanoparticles, the surface is covered with organic ligands that can direct growth and attachment, provide stability, and impart functionality.[11] Extensive work has gone into understanding the composition of the ligand shell and binding of the ligands to the nanoparticle surface to better tune the surface chemistry of the nanocrystal for desired applications.[12] Mapping ligand binding positions on nanocrystals is still challenging[13] as current methods of overgrowth,[14,15] nuclear magnetic resonance spectroscopy,[16−18] scanning tunneling microscopy,[19,20] and dry transmission electron microscopy (TEM)[21−24] all have limitations, and *in situ* observations of the effects of ligands on *in situ* dynamics are currently lacking.

In situ liquid cell electron microscopy of colloidal nanoparticles enables the observation of nanoscale phenomena in native liquid environments. Encapsulating liquid solutions between thin membranes such as silicon nitride and graphene protects the samples from the vacuum of the TEM column during measurement while maintaining the high spatial resolution of the electron microscope.[25,26] Both the silicon nitride and graphene liquid cells have yielded insights into nanocrystal growth,[27−30] attachment,[26] assembly,[31,32] and movement in solution.[33,34] Some of the dynamics observed in the liquid cell have been attributed to ligands in the system,[25,35−38] which suggests liquid cell electron microscopy may be a useful tool in studying the ligand shell.

The recent development of a controllable oxidative etching environment in the graphene liquid cell provides a means for quantitatively observing how ligands affect the etching of nanocrystals and, indirectly, where the ligands are binding.

Received: April 29, 2020
Accepted: July 30, 2020
Published: July 30, 2020

Downloaded via UNIV OF CALIFORNIA BERKELEY on February 16, 2021 at 19:09:08 (UTC).
See https://pubs.acs.org/sharingguidelines for options on how to legitimately share published articles.

© 2020 American Chemical Society

https://dx.doi.org/10.1021/acsnano.0c03601
ACS Nano 2020, 14, 10239–10250

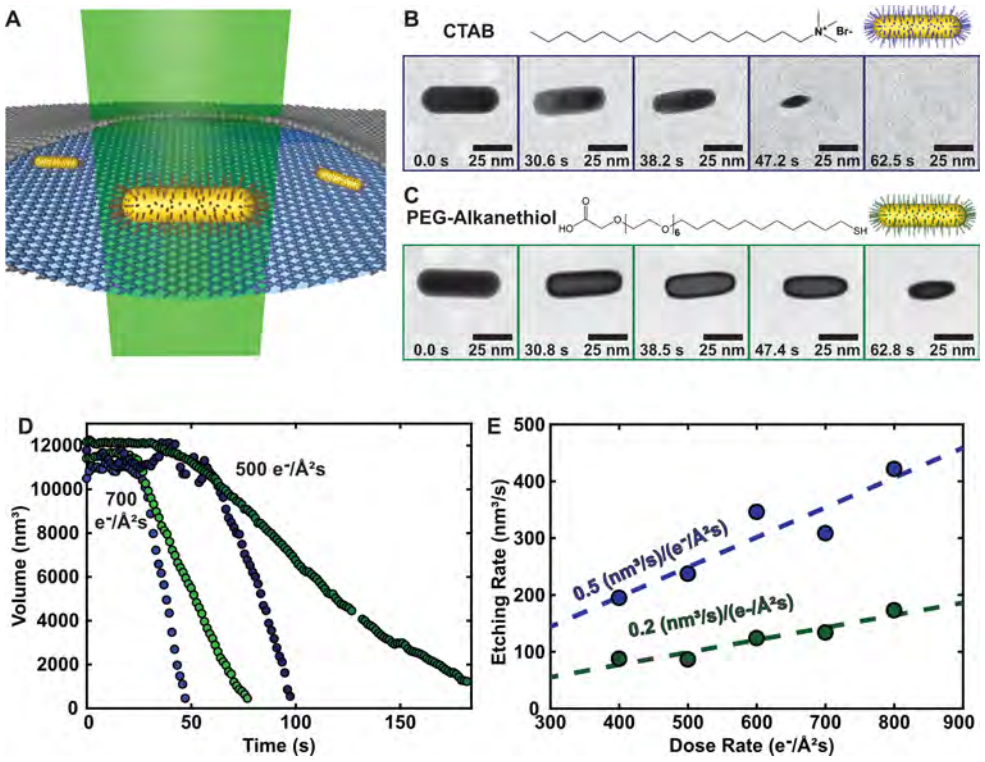

Figure 1. Volume trajectories of etching gold nanocrystals with different surface ligands. (A) Schematic of the graphene liquid cell with gold nanorods, imaged by the electron beam. (B) Images from a representative trajectory of an etching gold nanorod with CTAB ligands. (C) Images from a representative trajectory of an etching gold nanorod with PEG-alkanethiol ligands. (D) Representative volume trajectories of etching gold nanorods with CTAB (blue) and PEG-alkanethiol (green) ligands. For each dose rate (500 $e^-/Å^2$ s in darker colors and 700 $e^-/Å^2$ s in lighter colors), the etching rate is slower for the nanorods with PEG-alkanethiol. (E) Both CTAB (blue) and PEG-alkanethiol (green) show a linear etching rate dependence on the dose rate, but the nanorods with PEG-alkanethiol etch more than two times slower. The etching rate values for CTAB in (E) are from previously published work.[41]

Aqueous gold nanocrystals can be oxidatively etched through a combination of preloaded $FeCl_3$ and electron beam-induced radiolysis species.[39,40] The electron beam dose rate determines the total concentration of highly oxidative radiolysis species,[41] and the $FeCl_3$ controls the chemical potential of the etching process.[42] This system enables observation of intermediate, kinetic shape transformations that quenching or drying techniques may fail to capture.[40]

Using graphene liquid cell TEM to monitor oxidative etching of gold nanorods with various ligand shell compositions, we observed the dynamic effects of ligands on nanocrystals in their native liquid environment. By exchanging the original CTAB ligands for poly(ethylene glycol)-alkanethiol ($HS-(CH_2)_{11}-(EG)_6-OCH_2-COOH$) ligands, we show that ligands influence the etching dynamics throughout the entire process. Anisotropic dissolution of gold nanocrystals with cysteine ligands bound preferentially to the tips[15,43,44] reveals the local effect of the ligands and the potential ability to map indirectly the differential ligand binding position propensities. The shape transformation of cysteine-capped nanorods is controlled by the competition between atom removal and diffusion of surface atoms and ligands. Finally, the *in situ* TEM observations are corroborated with ensemble studies of the etching reactions in a flask. Utilizing graphene liquid cell electron microscopy to observe the effects of ligands on nanocrystal dynamics provides a tool for understanding the surface chemistry of nanocrystals and the effect of ligands on shape transformations.

RESULTS AND DISCUSSION

Etching of Nanorods with PEG-alkanethiol. Graphene liquid cell imaging techniques allow individual nanocrystal shape and volume trajectories to be tracked with the high spatial resolution of the electron microscope in the colloidal nanocrystals' native liquid environment (Figure 1A). A controllable etching system for aqueous gold nanocrystals using a combination of preloaded $FeCl_3$ and oxidative species generated through radiolysis of water by the electron beam has been previously developed with an understanding of the complex chemical environment occurring during the process.[39−42] Loading presynthesized gold nanocrystals for this etching process provides a known initial three-dimensional shape and composition of the ligand shell. The initial encapsulated solution contains as few excess CTAB ligands as possible, as excess CTAB ligands have been previously correlated with undesirable iron oxide formation.[41] Information such as shape and size can be extracted from the electron microscopy videos using image analysis. With this model system, the effects of ligands on nanocrystal etching can be investigated on the single nanoparticle level.

The ability of graphene liquid cell etching to detect modifications in ligand composition was tested by comparing the etching rates of gold nanorods before and after ligand exchange to PEG-alkanethiol. The initial gold nanorods were synthesized with a CTAB ligand shell following previously reported synthetic procedures.[45,46] Extensive characterization work in the literature on CTAB-coated gold nanorods has shown that CTAB binds to the gold surface through an

https://dx.doi.org/10.1021/acsnano.0c03601
ACS Nano 2020, 14, 10239−10250

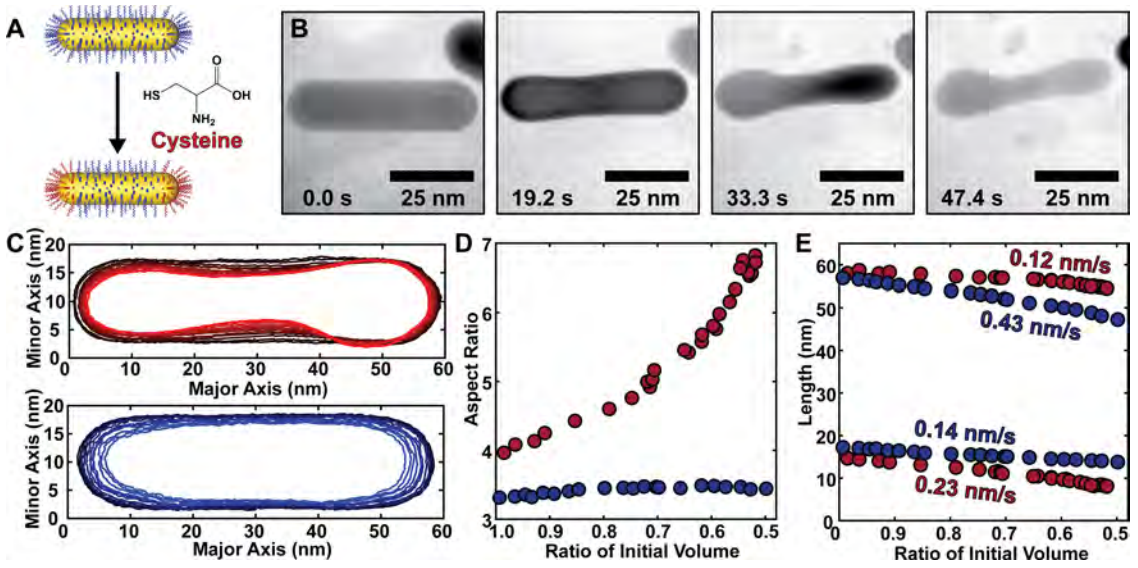

Figure 2. Etching in the graphene liquid cell reveals location-specific ligand binding. (A) Cysteine preferentially binds to the tips of the gold nanorod. (B) Representative images from cysteine-capped gold nanorod etching in a graphene liquid cell. (C) Outlines of a gold nanorod etching with cysteine (red) and without cysteine (blue). Darker outlines correspond to earlier times. Cysteine slows etching at the tips. (D) The aspect ratio of the nanorods during the etching process. The aspect ratio stays relatively constant for nanorods without cysteine (blue) while increasing sharply when cysteine ligands are present (red). (E) Etching rate of the major and minor axis. Without cysteine, the etching rate is three times faster at the tips, while cysteine adjusts the etching rate to be two times faster at the sides.

electrostatic interaction between the ammonium headgroup and the gold surface, with the tail forming an interdigitated bilayer.[47,48] To induce a quantitative difference in etching rate, the CTAB ligands were replaced by ($HS\text{-}(CH_2)_{11}\text{-}(EG)_6\text{-}OCH_2\text{-}COOH$) ligands. The ligand-exchange procedure followed previously reported protocols for this PEG-alkanethiol ligand and is similar to methods used to exchange CTAB ligands to thiolated DNA ligands on gold nanocrystals, using a large excess of PEG-alkanethiol ligand to ensure uniform exchange to coat the entire nanorod surface.[49] Thiolated polymer ligands have been extensively studied for biological applications and nanoparticle assembly,[50−52] and poly(ethylene glycol) ligands have been shown to protect the nanocrystals from degradation.[53,54] In this study, PEG-alkanethiol ligands with only six repeating ethylene glycol units were used to avoid the formation of a full polymer shell that would have completely prevented any etching of the nanocrystals. The ligand exchange from CTAB to PEG-alkanethiol ligands was characterized by elemental analysis following previous literature procedures[55−57] (see Supporting Information). Tracking the etching rates and shape trajectory of the gold nanorods with CTAB and PEG-alkanethiol can provide information about how ligands behave in the highly reactive graphene liquid cell environment.

When etched under similar conditions, the gold nanorods with PEG-alkanethiol ligands etch at less than half the rate of gold nanorods with CTAB. Qualitatively, upon undergoing oxidative etching at the same electron beam dose rate and initial size, the gold nanorods follow a relatively similar shape trajectory, but complete etching of the PEG-alkanethiol-coated nanorods takes roughly twice as long as the CTAB-coated nanorods (Figure 1B,C). Using image analysis techniques, the volume trajectories can be tracked and compared for similarly sized nanorods with CTAB and PEG-alkanethiol ligands (Figure 1D). Initially, all of the nanorods experience an induction period with no etching, and this is consistent with previous reports of hydrogen bubbles acting as a sacrificial reductant.[41] The time for the induction period is only dependent on the electron beam dose rate and not the ligands on the nanocrystal, providing further support that the induction period is related to the chemistry in the solution and not the nature of the nanocrystals. After the induction period, both PEG-alkanethiol-coated (green) and CTAB-coated (blue) nanorods have a constant etching rate with faster etching at higher electron beam dose rates (Figure 1D). At similar electron beam dose rates, however, the PEG-alkanethiol-coated nanorods etch slower. The etching rates of PEG-alkanethiol-coated nanorods show a linear dependence on the electron beam dose rate like CTAB-coated nanorods,[41] but PEG-alkanethiol-coated rods consistently etch at less than half the rate of the CTAB-coated nanorods (Figure 1E). The slower etching indicates that the PEG-alkanethiol ligand is protecting the nanorods from oxidative etching in the graphene liquid cell.

The reproducible and measurable difference in etching rates between gold nanorods with PEG-alkanethiol and CTAB indicates that ligands are still active during graphene liquid cell reactions. The effects of ligands persist throughout the entire etching process, and no convergence in etching behavior between CTAB-coated and thiol-capped nanocrystals was observed. This suggests the interaction between the ligands and the nanoparticle surface is maintained throughout the etching process, with ligands able to diffuse along the surface while the nanocrystal shrinks in size. Although it is not necessarily intuitive that ligands would survive the beam-generated radical species, there is a literature precedent for ligands affecting nanocrystal dynamics in liquid cell electron microscopy experiments.[27,36−38,58] The change in ligand composition in this experiment does not affect the induction period, suggesting the surface ligands are not affecting that chemical aspect of the liquid cell environment. To further probe whether the ligands affect etching locally on the nanocrystal, ligands with preferential binding to specific locations on the nanocrystal were investigated.

https://dx.doi.org/10.1021/acsnano.0c03601
ACS Nano 2020, 14, 10239−10250

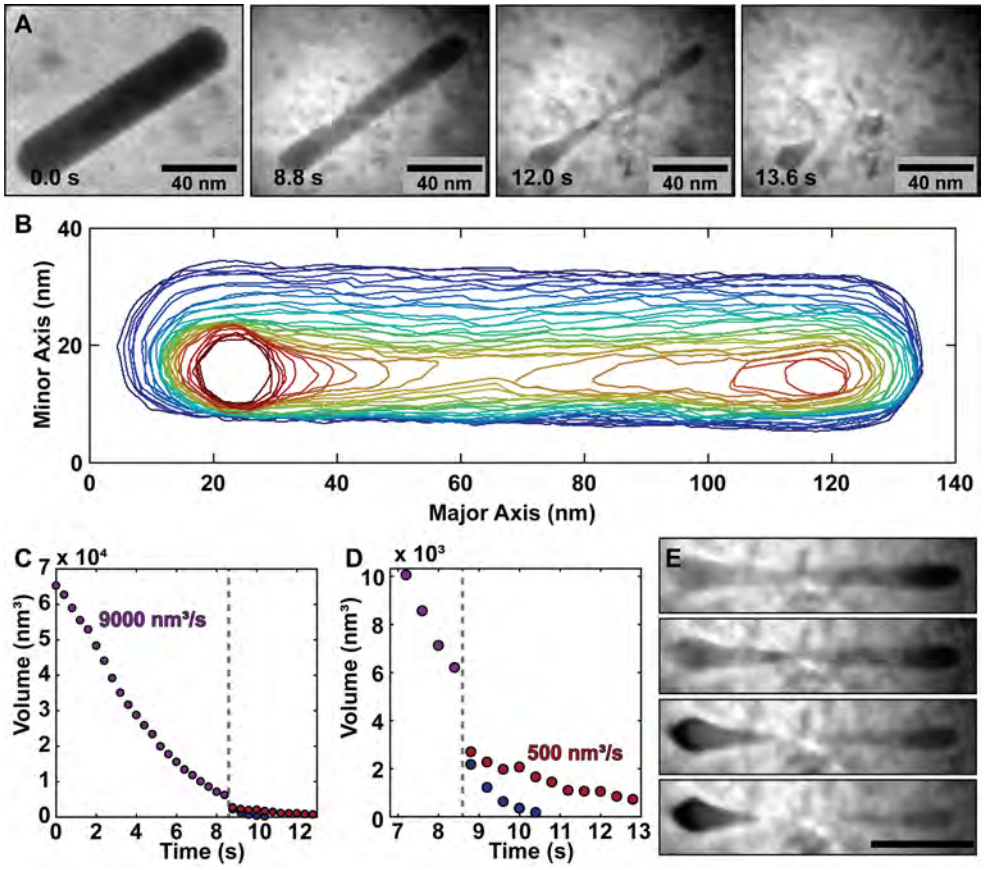

Figure 3. Observing the fragmentation of a gold nanorod into two smaller spheres during the etching process. (A) Representative images from the etching cysteine-capped nanorod that undergoes fragmentation. (B) Outlines from the etching cysteine-capped nanorod. Etching proceeds preferentially at the center of the rod, and the nanorod eventually breaks into two smaller nanoparticles at the center. These smaller nanoparticles transform to spherical shapes while continuing to etch. (C) The volume trajectory of the etching nanorod. The purple trajectory represents the nanorod before fragmentation, and the red and blue trajectories represent the volume of the two nanoparticles after fragmentation. The gray dotted line represents the fragmentation event. (D) At the fragmentation event, the etching rates slow down by more than an order of magnitude, due to the cysteine on the tips. (E) Images immediately before and after the breaking event. Scale bar is 40 nm, and frames are 0.4 s apart.

Etching of Cysteine-Capped Gold Nanorods. Cysteine has previously been shown to preferentially bind to the tips of gold nanorods,[54] so etching of cysteine-capped nanorods should induce asymmetric shape trajectories due to local ligand-dependent etching rates. Evidence for selective binding of cysteine to the tips of gold nanorods includes previous overgrowth studies[15] and end-to-end assembly of gold nanorods in the presence of cysteine ligands.[43,44] Nanorods with CTAB coverage have been shown to have lower ligand density at the tips,[24] and the lower ligand coverage at the tips of CTAB-coated nanorods enables cysteine to bind through their thiol functional group preferentially on the tips.[43] After addition of cysteine, the gold nanorods likely have CTAB on the sides and cysteine ligands on the tips, as characterized by elemental analysis (see Supporting Information). For this work, cysteine-capped nanorods refer to nanorods with low amounts of cysteine that cover the tips but not the sides of the nanorod. Based on PEG-alkanethiol results from above that showed a change in etching rate after ligand exchange, the preferential binding of cysteine to the gold nanorod tips would be expected to modulate the etching rate locally at the nanorod tips, leading to anisotropic shaped trajectories.

When etched under similar graphene liquid cell conditions, gold nanorods with low amounts of cysteine etched preferentially on the sides, leading to thinner nanorods or dumbbell shapes (Figure 2B). The full etching trajectory was difficult to capture because the cysteine-capped nanorods etched much slower due to lack of etching at the tips, requiring a higher electron beam dose rate for timely etching. Higher electron beam dose rates have previously been shown to increase the oxidative etching rate without changing the shape trajectory.[41] The higher dose rate, however, did seem to cause faster drying of the liquid cell, possibly due to greater damage on the graphene. The outlines for each frame of a representative etching video for a cysteine-capped nanorod (red) and CTAB-only nanorod (blue) show significant differences in shape trajectory (Figure 2C). The darker outlines are the earlier times, and the smallest volume outlines for the CTAB-only and cysteine-capped nanorods are at the same percentage of the initial nanorod volume. The aspect ratio provides a quantitative metric for tracking the ratio of major axis length to width at the center of the nanorod (Figure 2D). While the aspect ratio stays relatively constant for nanorods with only CTAB, the aspect ratio of cysteine-capped nanorods increases sharply during etching. The etching rates of the major axis and minor axis also show that cysteine has altered the shape trajectory (Figure 2E). For the CTAB-only nanorod (blue), the tips etch roughly three times faster than

https://dx.doi.org/10.1021/acsnano.0c03601
ACS Nano 2020, 14, 10239−10250

the sides to maintain the aspect ratio of three, but the cysteine-capped nanorod etches about 2 times faster on the sides than the tips. The faster etching rate at the CTAB-coated nanorod tips is likely due to lower CTAB ligand density at the tips.[24] A higher electron beam dose rate was used for the cysteine-capped, CTAB-sides nanorods to induce faster etching, so the side etching rate was higher for cysteine-capped than the CTAB-coated nanorods. Interestingly, despite the higher electron beam dose rate, the cysteine-capped nanorods still had a tip etching rate that was three times slower. The anisotropic etching behavior for the cysteine-capped nanorods is consistent and reproducible (Figures S2 and S3). Since the site-specific ligand binding of cysteine induces differences in the etching shape transformation, the effect of ligands on etching in the graphene liquid cell has a local component.

If a greater amount of cysteine is added to the gold nanorod solution, presumably all preferential tip binding sites are saturated and cysteine will bind to the sides of the nanorod. The etching trajectory in the graphene liquid cell reflects this change in cysteine ligand coverage of the gold nanorod surface with slower etching on both the sides and tips (Figure S4). The shape trajectory with full cysteine coverage is very similar to nanorods with only CTAB or PEG-alkanethiol, but the aspect ratio goes down with full cysteine coverage due to etching rates at the sides being seven times slower than the etching rate at the tips. For CTAB-coated nanorods, the ratio of tip to side etching rates is usually equal to the aspect ratio. Adding cysteine to the ligand shell likely changes the energetics and sterics of the nanocrystal surface, leading to a modulation of removal probabilities for tip or side atoms and a different ratio of etching rates. Due to the extremely slow etching of the full cysteine coverage gold nanorods, the electron beam dose rate was increased by 2−3 times compared to the dose rates used to etch nanorods with CTAB or PEG-alkanethiol. The linear fit for etching rate as a function of dose rate for full cysteine coverage nanorods had a slope of 0.03 $(nm^3/s)/(e^-/Å^2/s)$, far less than the slopes for nanorods with CTAB-only (0.52 $(nm^3/s)/(e^-/Å^2/s)$) and PEG-alkanethiol (0.22 $(nm^3/s)/(e^-/Å^2/s)$) (Figure S5). Graphene liquid cell etching shows isotropic and anisotropic etching for full cysteine coverage and cysteine-capped nanorods, respectively, indicating that graphene liquid cell etching could be used to infer preferential binding maps for ligand coverage and to examine ligand diffusion on nanocrystals.

The preferential etching at the sides of the cysteine-capped nanorods suggests there should be a point where the nanorod breaks apart at the center. Etching longer, higher aspect ratio cysteine-capped nanorods leads to fragmentation when the width becomes small, leading to two smaller nanoparticles (Figure 3A). The fragmentation event itself is challenging to observe because it occurs quickly, but the behavior is reproducible (Figures S6−S8). The transformation process can be separated into the initial etching from the sides of the nanorod, the fragmentation event, and etching of the remaining nanoparticles (Figure 3B). The oxidative etching from the sides behaves similarly to the other cysteine-capped nanorod etchings, with a constant volumetric etching rate (Figure 3C) and faster etching at the sides than the tips of the nanorod (Figure S9). This difference in site-specific etching rates leads to a rapid increase in the aspect ratio (Figure S10). The volumetric etching rate for this gold nanorod is higher than the previous cysteine-capped nanorods due to a higher electron beam dose rate and larger initial nanorod size. The larger nanorod allows for oxidative species from a larger region of the liquid cell pocket to interact with the nanorod. Once the nanorod has split, the etching rate slows down by over an order of magnitude, potentially due to reorganization of the cysteine on the two high curvature spherical nanoparticles (Figure 3D). Etching of cysteine-capped nanorods allows *in situ* observation and study of the breaking process for nanoscale gold rods.

The fragmentation of the thin cysteine-capped nanorod into two spheres happens rapidly (yellow to red outlines in Figure 3B). The exact moment of fragmentation is difficult to capture with the frame rate and spatial resolution of the TEM used in this experiment, but the nanorod becomes visibly skinnier at the center before fragmenting into two teardrop nanoparticles (Figure 3E). Based on the constant side etching rate of 2.6 nm/s, the width of the nanorod should only decrease by 1 nm/frame. Interestingly, the width of the nanorod in the last frame before the breaking event is 3 nm, which is larger than the expected 1 nm. The jump from a width of 3 nm to separation is likely due to a combination of surface diffusion and increased etching rate from undercoordinated gold atoms on the high curvature surface. This fragmentation of a crystalline gold nanorod can be compared to breaking at a grain boundary (Figure S11). In a different TEM video, initially separated gold nanorods can be observed moving toward each other, attaching, and then continuing to etch. Eventually, the attachment point becomes thin, and the two nanorods break apart again. The breaking behavior at the grain boundary appears qualitatively similar to single nanocrystal breaking at this spatial resolution and frame rate, but future research could investigate differences in the breaking mechanisms.

This fragmentation phenomenon is an example of a Raleigh instability. Thin wires are inherently less stable, owing to the simple geometric argument that a cylinder has more surface than two spheres of the same volume. This instability leads to diffusion of atoms, as the nanostructure rearranges to a lower energy configuration. More than 100 years ago, an analytical model for this rearrangement was applied to liquid systems,[59,60] and this analysis was extended to solid systems more than 50 years ago.[61,62] Raleigh instabilities in thin nanowires have become an active area of research in the microelectronics industry, and there are many examples using heating or charging to break down nanowires and nanoparticles.[63−66] As the cysteine-capped nanorods thin in the graphene liquid cell, it becomes energetically favorable for the rod to split into two smaller spheres. As the pinch-off time goes as the fourth power of the wire radius,[61,62] the breaking event happens rapidly. The convolution of oxidative etching and diffusion of surface atoms on the etching cysteine-capped nanorods makes it difficult to apply analytical models for Rayleigh instabilities.[67] The oxidative etching of the gold nanorods is a case of a Rayleigh instability where surface atom diffusion and removal are competitive and both contribute to the resulting shape transformation.

Evidence for the surface energy influence on the restructuring also comes from observations after the cysteine-capped nanorods fragment. The two resulting nanoparticles reshape into spheres while continuing to be etched. The breaking event leaves the nanoparticles as teardrop shapes, but the nanoparticles rapidly reshape to spheres to minimize surface energy (Figure 4A). The pathway to spheres involves preferential etching of atoms at positions of higher curvature, but surface diffusion may also contribute to the reshaping (Figure 4B). As the major axis of the nanoparticle is rapidly

https://dx.doi.org/10.1021/acsnano.0c03601
ACS Nano 2020, 14, 10239−10250

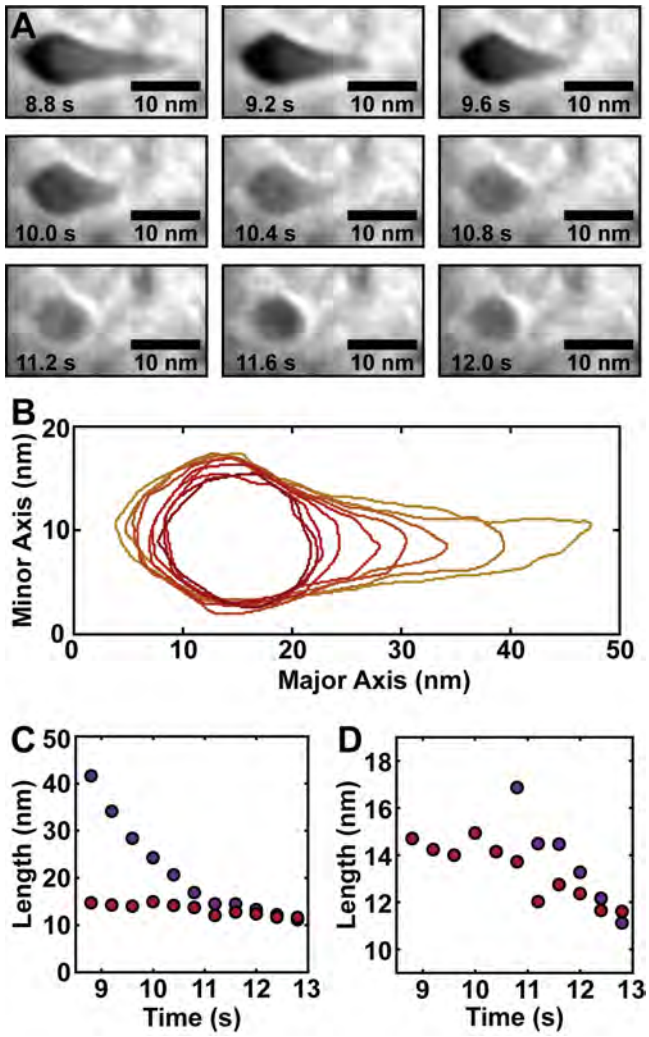

Figure 4. Nanoparticle transformation to a sphere after the fragmentation event. (A) Images from the nanoparticle after the fragmentation event in Figure 3 as it transforms to a sphere while continuing to etch. (B) Outlines from images in (A). Colors match Figure 3B. (C) Length of the major (purple) and minor (red) axis after the breaking event. The major axis decreases rapidly until the nanoparticle forms a spherical shape. (D) Expansion on the minor axis length. The minor axis increases slightly around 10 s as the nanoparticle reshapes itself into a sphere. This is notable because the nanoparticle is still etching, indicating the rearrangement of gold atoms on the surface happens on a time scale that is competitive with the etching rate.

decreasing in length (Figure 4C), there are a few frames where the minor axis seems to increase slightly, but it is difficult to definitively conclude that surface diffusion caused the minor axis to increase due to the small increase and fluctuations in contrast of the TEM images. Previously reported measurements of gold atom diffusion on a gold electrode with no electric bias in an acidic solution containing chlorine ions estimated a surface diffusion constant of 25 nm^2/s, or for comparison, 10 nm^2/frame in this liquid cell experiment.[68] The system in the graphene liquid cell is substantially more complicated with ligands, etching, and ill-defined surface structure, but the reported surface diffusion constant of gold atoms suggests that for these small nanoparticles, surface diffusion could be competitive with atom removal in controlling the shape transformation. After the nanoparticle becomes spherical, the etching rate decreases by more than an order of magnitude compared to the volumetric rate during side etching of the nanorod, from 9000 to 500 nm^3/s. Cysteine from the tips of the original nanorods may be reorganizing to cover the smaller, highly curved nanosphere. Then, the entire nanosphere etches at the slow rate previously observed for the tips of the cysteine-capped nanorods. The ability to observe the effects of ligand and atom diffusion using dynamic graphene liquid cell electron microscopy experiments will aid in understanding and quantifying these nanoscale phenomena.

***Ex Situ* Etching of Ligand-Exchanged Gold Nanorods.** Correlating *in situ* electron microscopy experiments with typical colloidal syntheses and reactions in a flask is important for validating the observed phenomena. Previous work has shown that the plasmon resonances of gold nanoparticles can be followed by UV−vis spectroscopy to compare etching dynamics induced by the electron beam in the graphene liquid cell with colloidal oxidative etching reactions using $FeCl_3$.[41] For gold nanorods, the energy of the longitudinal surface plasmon resonance (LSPR) is determined by the aspect ratio of the nanorod.[69] Thus, observing the extinction spectra of a solution of cysteine-capped gold nanorods during etching provides insight into the average trajectory and the reproducibility of the shape transformations seen in the graphene liquid cell.

The etching of ligand-exchanged gold nanorods can be induced without the electron beam using a solution of $FeCl_3$ and CTAB. Previous work has shown that etching gold nanorods with CTAB ligands leads to blue-shifted or constant LSPRs, depending on the $FeCl_3$ concentration.[41,69,70] For gold nanorods with PEG-alkanethiol ligands, the etching occurs slower than CTAB-coated nanorods at the same etching conditions, similar to the graphene liquid cell results (Figure S14). The LSPR of cysteine-capped nanorods red shifts and decreases in intensity, indicating an increase in aspect ratio as etching occurs preferentially at the sides (Figure 5A). The etching reaction was stopped by rapidly diluting the solution, and the resulting sample was precipitated by centrifugation to perform TEM imaging and quantitative analysis on the intermediate etching structures. The LSPR shifts roughly 150 nm from the initial gold nanorods to the etched structures (Figure 5B). The final extinction spectrum has a lower intensity likely because some nanorods were etched to nothing or to small spheres that were lost during the centrifugation process. Dry TEM images show significant etching at the sides of the cysteine-capped nanorods (Figures 5C and S12). Quantitative image analysis confirms a decrease in the size of the gold nanoparticles and an increase in aspect ratio (Figure S13). *Ex situ* etching experiments of nanorods with greater amounts of cysteine suggest corroboration of the extremely slow etching seen during *in situ* observations, but aggregation renders the analysis inconclusive (Figures S18 and S19). Reproducing the side etching of cysteine-capped gold nanorods and the slower etching of PEG-alkanethiol and cysteine-covered gold nanorods in a flask confirms that the observed graphene liquid cell dynamics are not artifacts of the environment or experimental technique.

Chemistry of Liquid Cell Environment. Although liquid cell TEM provides no direct information about the ligands and their stability in the radiolytic environment, the extensive literature on interactions of molecules and radiolysis products suggests potential ligand stability. A definitive understanding of ligand chemistry in the radiolytic liquid cell environment will

https://dx.doi.org/10.1021/acsnano.0c03601
ACS Nano 2020, 14, 10239−10250

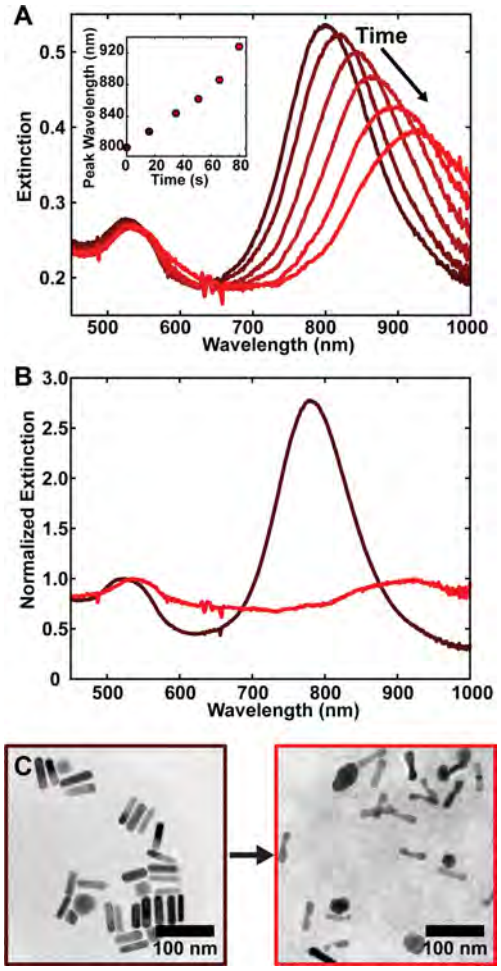

Figure 5. Correlative *ex situ* etching of cysteine-capped gold nanorods. (A) The etching of cysteine-capped gold nanorods can be followed by their plasmon resonances due to the changing aspect ratio of the nanorod. The red shift in the LSPR indicates an increasing aspect ratio as the nanorod etches from the sides. (B) Extinction spectra of the initial gold nanorods and cysteine-capped gold nanorods after quenching of etching. (C) Representative TEM images of cysteine-capped gold nanorods before and after etching. Significant etching into the sides of the nanorods indicates protection of the nanorod tips by cysteine.

have to await improved analytical capabilities and reaction network simulations. It is expected that ligands would react with the radiolysis species, but it is clear from the data that the ligands, or any resulting ligands after reactions, maintain the differential etching rate. All components of the ligand including the counterion likely influence the etching, but we do not expect any of the components to be directly etching the gold nanocrystals. Future mechanistic work investigating the influence of each component of the ligands including the halides, carbon backbone, and headgroup on the reaction chemistry would provide an even deeper understanding of this process. Literature on the reactions of radiolysis species with CTAB, cysteine, and PEG-alkanethiols can, however, provide a starting point for understanding the chemistry of the ligands in the liquid cell.

While the exact chemistry of CTAB in a radiolytic environment is not fully understood, a variety of radiolytic aqueous nanoparticle syntheses utilize CTAB as a ligand for colloidal stability and shape control.[71,72] Experiments investigating the reactivity of CTAB with aqueous solutions of isolated radiolysis products have shown a low reactivity with hydrated electrons but higher reactivity with the hydroxyl radical and hydrogen radical.[73] The hydroxyl radical removes a hydrogen from the alkyl chain, resulting in an alkyl radical.[74] For the liquid cell studies in this work, polymerization would be expected to cause a decrease in etching rate, as the polymer protects the nanoparticle from the liquid environment. Since a constant etching rate is observed throughout etching, it is possible that subsequent reactions of the alkyl radical with hydrogen radical and H^+ may be limiting the concentration of alkyl radicals present at any time. Conducting the liquid cell experiments at a low pH provides excess H^+ ions, potentially healing CTAB ligands damaged by the hydroxyl radical.

For cysteine, the fastest reactions with radiolysis species happen at the thiol group. Hydrated electrons can rapidly react with the thiol, yielding a negatively charged hydrogen sulfide ion and a $HO_2CCH(NH_2)CH_2$ radical.[75,76] In the oxidative environment used in this work, the hydrated electron concentration is suppressed,[41] making this cysteine reduction pathway unlikely. A more likely pathway would be the oxidative hydroxyl radical preferentially attacking the thiol and removing a hydrogen to yield a $HO_2CCH(NH_2)CH_2S$ radical.[75,76] This study, however, found that cysteine decreased the local etching rate in a constant manner throughout the etching trajectory, so the cysteine is either robust to the hydroxyl radical under the liquid cell conditions or altered in a way that does not change the cysteine ligand's effect on etching. The thiol headgroup of cysteine is bound to the gold surface, so it may be harder for the hydroxyl radical to break that strong gold−sulfur interaction to react with the headgroup to form a cysteine radical. Even if hydroxyl radical was able to react with the bound cysteine to form a radical, creation of the cysteine radical leads to disulfide formation in the presence of oxygen (see Supporting Information for reaction pathway). The disulfide also preferentially binds to gold nanorod tips,[14] so the local effect of the ligand on etching may be maintained. Although we have no direct evidence of the reactions of cysteine with radiolysis species, the counterintuitive ability of cysteine to consistently influence the nanoparticle dynamics in the liquid cell can be rationalized by the reaction mechanisms of cysteine and radiolysis species.

The gold nanocrystals with PEG-alkanethiol ligands also exhibit a constant etching rate during etching, and literature on PEG in radiolytic environments can provide reasons behind the ligands' persistence. The alkane part of the PEG-alkanethiol ligand likely behaves similarly to the carbon backbone of CTAB, with the same rationale for stability being applicable. For the PEG portion of the ligand, hydrogen atoms at the α position are most vulnerable, resulting in a radical species.[77] If no oxygen is present in solution, PEG radicals can react with adjacent radicals to form a polymer.[78] The liquid cell solutions in this study were made in ambient conditions with oxygen, and no polymerization was observed by image contrast or decreased etching rates in the TEM. When oxygen is present, the PEG radical can react with oxygen to induce cleaving.[79] If a measurable amount of cleaving of the PEG units occurred during the etching experiments, a reasonable hypothesis would be an increase in etching rate due to the shorter chain. An interesting follow-up to this study could investigate the effect of similar ligands of differing lengths on etching rate. Cleavage of the entire PEG portion of the ligand would have left an alkyl chain that was shorter than

https://dx.doi.org/10.1021/acsnano.0c03601
ACS Nano 2020, 14, 10239−10250

CTAB, and this does not seem consistent with the experimentally slower etching observed for PEG alkanethiol. A potential explanation for the observed stability of PEG-alkanethiol ligands is the much greater concentration of hydrogen (in the form of H_2, H^+, and H radical) than oxygen in liquid cell TEM experiments.[80] Previous work has shown that PEG in low pH solutions experiences less polymerization under irradiation,[81] which could be due to the high hydrogen concentration suppressing the PEG radical concentration. Probing the local effect of ligands on nanoparticle etching dynamics in the liquid cell requires the ligands to have differentiated and constant influence during the process, and although there is no direct evidence of the exact reaction pathways, the previous work in this area shows plausible ways that the ligands could persist in the reactive liquid cell environment.

Before using graphene liquid cell TEM to study other ligand compositions, a variety of factors including chemistry, solvent, and temperature need to be considered. Although the CTAB, PEG-alkanethiol, and CTAB-cysteine ligand shells in this study seem to have a consistent impact on etching despite the electron beam, the chemistry of other surfactants may be more reactive. For example, control of pH and pOH is not fully understood in the graphene liquid cell, so pH sensitive ligands may undergo changes during observation in the TEM. Ligands that are easily cross-linked under electron beam irradiation would likely polymerize during graphene liquid cell experiments leading to structural changes in the ligand shell. Water was used as the solvent in this study, but other solvents have been previously shown to work in the graphene liquid cell. Changing the solvent may require tuning of the liquid composition to ensure proper pocket sealing, and the experiment would need to account for different solvent-dependent electron beam-induced chemistry. The temperature in liquid cell TEM has previously been shown to not increase by more than a few degrees Celsius during electron beam irradiation.[82] If elevated or depressed temperatures are desired, the graphene liquid cell can fit in most commercial heating and cooling holders. Validating the local temperature for a graphene liquid cell in a temperature-controlled holder would be challenging, but an interesting area of future research. Every system is different and will require optimization for proper pocket sealing and etching chemistry, but the graphene liquid cell should be extendable for studying a variety of other ligand–nanocrystal systems.

CONCLUSION

Observing the effects of ligands on etching of nanocrystals with liquid cell electron microscopy provides insight into the mechanisms of nanoscale shape transformations and processes like Rayleigh instabilities, but it also will enable further studies of nanocrystal ligands. This work demonstrates that ligands can still be active in the highly reactive environment of graphene liquid cell electron microscopy, and additional research could go into further understanding the stability of ligands in the liquid cell. More in-depth comparisons on ligand effects in silicon nitride *versus* graphene liquid cell[83] and growth *versus* etching, especially using *in situ* spectroscopic techniques such as EELS, would yield further information about ligand coverage and the chemical environment during liquid cell electron microscopy experiments. From a colloidal chemistry perspective, the ability to map out where ligands are binding to a nanocrystal using graphene liquid cell etching would aid in understanding ligand–nanocrystal interactions. This technique could be used to investigate facet specific binding, and results from these experiments could be useful in screening and mapping where different ligands are binding on various facets for nanocrystal assembly and other applications.[84,85] Mixed ligand shells could be studied with this system to distinguish patchy and uniform coverage or measure the diffusion of ligands on a nanocrystal. *In situ* etching also provides information about the stability of nanocrystal shapes, facets, and surface chemistry which could be useful for development of longer lasting catalysts and biomedical treatments.[86,87] By utilizing the understood system of oxidative etching in graphene liquid cell TEM, the ligand shell and its effect on nanocrystal dynamics can be studied on the nanoscale to yield insight for further synthetic development and applications.

METHODS

Synthesis of Single Crystalline Gold Nanorods. Single crystalline gold nanorods were synthesized following previously reported seeded growth methods.[45] Briefly, 0.3 mL of ice cold 0.01 M $NaBH_4$ was added to a solution of 5 mL of 0.1 M CTAB and 0.125 mL of 0.01 M $HAuCl_4$ and vigorously stirred for 2 min. After 30 min, 24 μL of this seed solution was added to a solution of 20 mL of 100 mM CTAB, 1 mL of 10 mM $HAuCl_4$, 0.3 mL of 10 mM $AgNO_3$, and 0.114 mL of 100 mM ascorbic acid. To synthesize the higher aspect ratio gold nanorods, the synthesis was modified following previously reported protocol.[88] The gold nanorods were spun down three times and redispursed in Millipore filtered water for CTAB-based etching experiments and future ligand exchanges. For elemental analysis, the gold nanorod reaction was scaled up by a factor of 51× to provide enough material for the analysis.

Exchanging to PEG-Alkanethiol Ligands. Ligand exchange from CTAB to PEG-alkanethiol followed previously reported synthetic protocols.[49] Gold nanorods were spun down and resuspended in 100 μL of 5.7 mM HS-$(CH_2)_{11}$-$(EG)_6$-OCH_2-COOH. Then, 2 mL of H_2O, 300 μL of 0.1% sodium dodecyl sulfate, and 600 μL of 1 M pH 8 phosphate buffer were added to the gold nanorod solution, resulting in a solution with 0.01% sodium dodecyl sulfate and 0.2 M phosphates buffered at pH 8 with 190 mM of PEG-alkanethiol ligand. The amount of nanorods in the solution can vary as long as the amount PEG-alkanethiol added is significantly in excess. The solution was sonicated for 10 s and then left to sonicate overnight at 35–40 °C. After overnight sonication, the solution was centrifuged three times and resuspended in 0.01% sodium dodecyl sulfate solution.

Adding Cysteine to Gold Nanorod Tips for Graphene Liquid Cell Experiments. Twenty-one μL of 1 nM gold nanorods was mixed with 4.5 μL of 1 mM cysteine and incubated for 14 h in the dark at room temperature. CTAB was not used in this exchange to avoid iron oxyhydroxide species from forming during liquid cell experiments.[41] For the nanorods with full cysteine coverage, 20 μL of 1 nM gold nanorods were mixed with 5 μL of 1 mM cysteine and incubated for 17 h in the dark at room temperature. Gold nanorod solutions with full cysteine coverage showed aggregation at the bottom of the micro test tube.

Graphene Liquid Cell Fabrication. The graphene liquid cells were fabricated following previous reported procedures.[39] Briefly, 3–5 layer graphene was transferred to holey, amorphous carbon, gold quantifoil TEM grids (SPI Supplies, 300 mesh, R1.2/1.3). These grids were used to encapsulate a solution of 38 mM $FeCl_3$, 8 mM HCl, 58 mM Tris buffer-HCl, and the gold nanorods of interest. All samples were imaged 30 min to 3 h after encapsulation.

TEM Imaging Conditions. All TEM imaging was performed on a FEI Tecnai T20 S-Twin TEM operating at 200 kV with a LaB_6 filament. Videos of nanocrystal dynamics were collected using a Gatan Orius SC200 camera utilizing a custom digital micrograph script with a full 2048 × 2048 readout with a binning of 2 pixels in each direction, at a nominal magnification of 71 kx resulting in a pixel resolution of

https://dx.doi.org/10.1021/acsnano.0c03601
ACS Nano 2020, 14, 10239–10250

1.5 Å/pixel. The exposure time was 0.5 s, with a readout time of 0.8 s, yielding a frame rate of 0.77 fps. The electron dose rate was calibrated using our previously reported method.[41,42] For the TEM electron beam dose rate calibration script, a conversion value of 6.7 counts/electron was used to convert CCD counts to electrons, consistent with our previous work.

***Ex Situ* Etching of Cysteine-Capped Nanorods.** A gold nanorod stock solution was redispersed in an aqueous solution of 10 μM cysteine and 0.1 M CTAB acidified with 0.1 mM HCl such that the OD was approximately 1, based roughly on a previously reported procedure.[15] The functionalization mixture was kept at 27 °C for 2 h. To remove excess cysteine, the solution was centrifuged twice, redispursing in 0.1 M CTAB acidified with 0.1 mM HCl. 500 μL of cysteine-capped gold nanorods at OD 0.6 were added to a quartz cuvette and placed inside the Shimadzu UV−vis spectrometer. Four μL of a solution of 0.2 M $FeCl_3$ in 0.021 M HCl was injected into the cuvette. The solution was mixed with a glass pipet, and extinction spectra were subsequently acquired. For TEM images, the reaction was quenched by dilution with 25 mL of water and then centrifuged.

ASSOCIATED CONTENT

Supporting Information

The Supporting Information is available free of charge at https://pubs.acs.org/doi/10.1021/acsnano.0c03601.

Video S1: Au nanorod with CTAB etching in 38 mM $FeCl_3$ at a dose rate of 500 $e^-/Å^2$ s (AVI)

Video S2: Au nanorod with CTAB etching in 38 mM $FeCl_3$ at a dose rate of 700 $e^-/Å^2$ s (AVI)

Video S3: Au nanorod with PEG-alkanethiol etching in 38 mM $FeCl_3$ at a dose rate of 500 $e^-/Å^2$ s (AVI)

Video S4: Au nanorod with PEG-alkanethiol etching in 38 mM $FeCl_3$ at a dose rate of 700 $e^-/Å^2$ s (AVI)

Video S5: Au nanorod with cysteine on tips etching in 38 mM $FeCl_3$ at a dose rate of 3200 $e^-/Å^2$ s (AVI)

Video S6: Au nanorod with cysteine on tips etching in 38 mM $FeCl_3$ at a dose rate of 3200 $e^-/Å^2$ s (AVI)

Video S7: Au nanorod with cysteine on tips undergoing a breaking event while etching (AVI)

CHNS elemental analysis of ligand composition on gold nanorods, ligand-radiolysis product chemistry in the liquid cell environment, supplemental figures, and additional *ex situ* experiments. The supplemental figures include additional analyzed trajectories of cysteine-capped and full cysteine coverage nanorods, additional images of nanorod breaking events, and additional TEM images and analysis of *ex situ* etched nanorods (PDF)

AUTHOR INFORMATION

Corresponding Author

A. Paul Alivisatos − *Department of Chemistry and Department of Materials Science and Engineering, University of California-Berkeley, Berkeley, California 94720, United States; Materials Sciences Division, Lawrence Berkeley National Laboratory, Berkeley, California 94720, United States; Kavli Energy NanoScience Institute, University of California-Berkeley and Lawrence Berkeley National Laboratory, Berkeley, California 94720, United States;* orcid.org/0000-0001-6895-9048; Email: paul.alivisatos@berkeley.edu

Authors

Matthew R. Hauwiller − *Department of Chemistry, University of California-Berkeley, Berkeley, California 94720, United States;* orcid.org/0000-0002-5448-6937

Xingchen Ye − *Department of Chemistry, University of California-Berkeley, Berkeley, California 94720, United States;* orcid.org/0000-0001-6851-2721

Matthew R. Jones − *Department of Chemistry, University of California-Berkeley, Berkeley, California 94720, United States;* orcid.org/0000-0002-9289-291X

Cindy M. Chan − *Department of Chemistry, University of California-Berkeley, Berkeley, California 94720, United States*

Jason J. Calvin − *Department of Chemistry, University of California-Berkeley, Berkeley, California 94720, United States;* orcid.org/0000-0001-8381-2466

Michelle F. Crook − *Department of Chemistry, University of California-Berkeley, Berkeley, California 94720, United States;* orcid.org/0000-0003-3550-0868

Haimei Zheng − *Department of Materials Science and Engineering, University of California-Berkeley, Berkeley, California 94720, United States; Materials Sciences Division, Lawrence Berkeley National Laboratory, Berkeley, California 94720, United States;* orcid.org/0000-0003-3813-4170

Complete contact information is available at: https://pubs.acs.org/10.1021/acsnano.0c03601

Notes

The authors declare no competing financial interest.

ACKNOWLEDGMENTS

The work was supported by the U.S. Department of Energy, Office of Science, Office of Basic Energy Sciences, Materials Sciences and Engineering Division, under contract no. DE-AC02-05-CH11231 within the Physical Chemistry of Inorganic Nanostructures Program (KC3103). Effort by H.Z. was partially supported by DOE BES, Materials Sciences and Engineering Division under Contract No. DE-AC02-05-CH11231 within the *in situ* TEM program (KC22ZH). M.R.J. acknowledges the Arnold and Mabel Beckman Foundation for a postdoctoral fellowship. C.M.C. acknowledges funding from the SMART Summer Research Program. We thank Elena Kreimer at the UC Berkeley College of Chemistry Microanalytical Facility for conducting the CHNS analysis. Justin Ondry and Mariana Verdugo are acknowledged for their useful conversations. The authors also acknowledge Negest Williams for her invaluable administrative support.

REFERENCES

(1) Lu, X.; Rycenga, M.; Skrabalak, S. E.; Wiley, B.; Xia, Y. Chemical Synthesis of Novel Plasmonic Nanoparticles. *Annu. Rev. Phys. Chem.* **2009**, *60*, 167−192.

(2) Li, A.; Zhang, P.; Chang, X.; Cai, W.; Wang, T.; Gong, J. Gold Nanorod@TiO2 Yolk-Shell Nanostructures for Visible-Light-Driven Photocatalytic Oxidation of Benzyl Alcohol. *Small* **2015**, *11*, 1892−1899.

(3) You, H.; Yang, S.; Ding, B.; Yang, H. Synthesis of Colloidal Metal and Metal Alloy Nanoparticles for Electrochemical Energy Applications. *Chem. Soc. Rev.* **2013**, *42*, 2880−2904.

(4) Jing, H.; Zhang, Q.; Large, N.; Yu, C.; Blom, D. A.; Nordlander, P.; Wang, H. Tunable Plasmonic Nanoparticles with Catalytically Active High-Index Facets. *Nano Lett.* **2014**, *14*, 3674−3682.

(5) Wu, B.; Zheng, N. Surface and Interface Control of Noble Metal Nanocrystals for Catalytic and Electrocatalytic Applications. *Nano Today* **2013**, *8*, 168−197.

(6) Huang, X.; El-Sayed, M. A. Plasmonic Photo-Thermal Therapy (PPTT). *Alexandria J. Med.* **2011**, *47*, 1−9.

(7) Ali, M. R. K.; Wu, Y.; El-Sayed, M. A. Gold Nanoparticle-Assisted Plasmonic Photothermal Therapy Advances towards Clinical Application. *J. Phys. Chem. C* **2019**, *123*, 15375.
(8) Khosla, K.; Wang, Y.; Hagedorn, M.; Qin, Z.; Bischof, J. Gold Nanorod Induced Warming of Embryos from the Cryogenic State Enhances Viability. *ACS Nano* **2017**, *11*, 7869−7878.
(9) Mubeen, S.; Lee, J.; Lee, W. R.; Singh, N.; Stucky, G. D.; Moskovits, M. On the Plasmonic Photovoltaic. *ACS Nano* **2014**, *8*, 6066−6073.
(10) Talapin, D. V.; Lee, J.-S.; Kovalenko, M. V.; Shevchenko, E. V. Prospects of Colloidal Nanocrystals for Electronic and Optoelectronic Applications. *Chem. Rev.* **2010**, *110*, 389−458.
(11) Burrows, N. D.; Lin, W.; Hinman, J. G.; Dennison, J. M.; Vartanian, A. M.; Abadeer, N. S.; Grzincic, E. M.; Jacob, L. M.; Li, J.; Murphy, C. J. Surface Chemistry of Gold Nanorods. *Langmuir* **2016**, *32*, 9905−9921.
(12) Boles, M. A.; Ling, D.; Hyeon, T.; Talapin, D. V. The Surface Science of Nanocrystals. *Nat. Mater.* **2016**, *15*, 141−153.
(13) Cheng, X.; Anthony, T. P.; West, C. A.; Hu, Z.; Sundaresan, V.; McLeod, A. J.; Masiello, D. J.; Willets, K. A. Plasmon Heating Promotes Ligand Reorganization on Single Gold Nanorods. *J. Phys. Chem. Lett.* **2019**, *10*, 1394−1401.
(14) Hinman, J. G.; Eller, J. R.; Lin, W.; Li, J.; Li, J.; Murphy, C. J. Oxidation State of Capping Agent Affects Spatial Reactivity on Gold Nanorods. *J. Am. Chem. Soc.* **2017**, *139*, 9851−9854.
(15) Kou, X.; Zhang, S.; Yang, Z.; Tsung, C.-K.; Stucky, G. D.; Sun, L.; Wang, J.; Yan, C. Glutathione- and Cysteine-Induced Transverse Overgrowth on Gold Nanorods. *J. Am. Chem. Soc.* **2007**, *129*, 6402−6404.
(16) Hens, Z.; Martins, J. C. A Solution NMR Toolbox for Characterizing the Surface Chemistry of Colloidal Nanocrystals. *Chem. Mater.* **2013**, *25*, 1211−1221.
(17) Marbella, L. E.; Millstone, J. E. NMR Techniques for Noble Metal Nanoparticles. *Chem. Mater.* **2015**, *27*, 2721−2739.
(18) Al-Johani, H.; Abou-Hamad, E.; Jedidi, A.; Widdifield, C. M.; Viger-Gravel, J.; Sangaru, S. S.; Gajan, D.; Anjum, D. H.; Ould-Chikh, S.; Hedhili, M. N.; Gurinov, A.; Kelly, M. J.; El Eter, M.; Cavallo, L.; Emsley, L.; Basset, J.-M. The Structure and Binding Mode of Citrate in the Stabilization of Gold Nanoparticles. *Nat. Chem.* **2017**, *9*, 890−895.
(19) Jackson, A. M.; Myerson, J. W.; Stellacci, F. Spontaneous Assembly of Subnanometre-Ordered Domains in the Ligand Shell of Monolayer-Protected Nanoparticles. *Nat. Mater.* **2004**, *3*, 330−336.
(20) Centrone, A.; Hu, Y.; Jackson, A. M.; Zerbi, G.; Stellacci, F. Phase Separation on Mixed-Monolayer-Protected Metal Nanoparticles: A Study by Infrared Spectroscopy and Scanning Tunneling Microscopy. *Small* **2007**, *3*, 814−817.
(21) Yang, J. A.; Murphy, C. J. Evidence for Patchy Lipid Layers on Gold Nanoparticle Surfaces. *Langmuir* **2012**, *28*, 5404−5416.
(22) Galati, E.; Tao, H.; Tebbe, M.; Ansari, R.; Rubinstein, M.; Zhulina, E. B.; Kumacheva, E. Helicoidal Patterning of Nanorods with Polymer Ligands. *Angew. Chem., Int. Ed.* **2019**, *58*, 3123−3127.
(23) Tao, H.; Chen, L.; Galati, E.; Manion, J. G.; Seferos, D. S.; Zhulina, E. B.; Kumacheva, E. Helicoidal Patterning of Gold Nanorods by Phase Separation in Mixed Polymer Brushes. *Langmuir* **2019**, *35*, 15872−15879.
(24) Janicek, B. E.; Hinman, J. G.; Hinman, J. J.; Bae, S. h.; Wu, M.; Turner, J.; Chang, H.-H.; Park, E.; Lawless, R.; Suslick, K. S.; Murphy, C. J.; Huang, P. Y. Quantitative Imaging of Organic Ligand Density on Anisotropic Inorganic Nanocrystals. *Nano Lett.* **2019**, *19*, 6308−6314.
(25) Zheng, H.; Smith, R. K.; Jun, Y. -w.; Kisielowski, C.; Dahmen, U.; Alivisatos, A. P. Observation of Single Colloidal Platinum Nanocrystal Growth Trajectories. *Science* **2009**, *324*, 1309−1312.
(26) Yuk, J. M.; Park, J.; Ercius, P.; Kim, K.; Hellebusch, D. J.; Crommie, M. F.; Lee, J. Y.; Zettl, A.; Alivisatos, A. P. High-Resolution EM of Colloidal Nanocrystal Growth Using Graphene Liquid Cells. *Science* **2012**, *336*, 61−64.
(27) Liao, H.-G.; Zherebetskyy, D.; Xin, H.; Czarnik, C.; Ercius, P.; Elmlund, H.; Pan, M.; Wang, L.-W.; Zheng, H. Facet Development during Platinum Nanocube Growth. *Science* **2014**, *345*, 916−919.
(28) Ahmad, N.; Wang, G.; Nelayah, J.; Ricolleau, C.; Alloyeau, D. Exploring the Formation of Symmetric Gold Nanostars by Liquid-Cell Transmission Electron Microscopy. *Nano Lett.* **2017**, *17*, 4194−4201.
(29) Hauwiller, M. R.; Zhang, X.; Liang, W.-I.; Chiu, C.-H.; Zhang, Q.; Zheng, W.; Ophus, C.; Chan, E. M.; Czarnik, C.; Pan, M.; Ross, F. M.; Wu, W.-W.; Chu, Y.-H.; Asta, M.; Voorhees, P. W.; Alivisatos, A. P.; Zheng, H. Dynamics of Nanoscale Dendrite Formation in Solution Growth Revealed through *In Situ* Liquid Cell Electron Microscopy. *Nano Lett.* **2018**, *18*, 6427−6433.
(30) Tan, S. F.; Bisht, G.; Anand, U.; Bosman, M.; Yong, X. E.; Mirsaidov, U. *In Situ* Kinetic and Thermodynamic Growth Control of Au-Pd Core-Shell Nanoparticles. *J. Am. Chem. Soc.* **2018**, *140*, 11680−11685.
(31) Luo, B.; Smith, J. W.; Ou, Z.; Chen, Q. Quantifying the Self-Assembly Behavior of Anisotropic Nanoparticles Using Liquid-Phase Transmission Electron Microscopy. *Acc. Chem. Res.* **2017**, *50*, 1125.
(32) Luo, B.; Kim, A.; Smith, J. W.; Ou, Z.; Wu, Z.; Kim, J.; Chen, Q. Hierarchical Self-Assembly of 3D Lattices from Polydisperse Anisometric Colloids. *Nat. Commun.* **2019**, *10*, 1815.
(33) Chee, S. W.; Anand, U.; Bisht, G.; Tan, S. F.; Mirsaidov, U. Direct Observations of the Rotation and Translation of Anisotropic Nanoparticles Adsorbed at a Liquid-Solid Interface. *Nano Lett.* **2019**, *19*, 2871.
(34) Chen, Q.; Cho, H.; Manthiram, K.; Yoshida, M.; Ye, X.; Alivisatos, a. P. Interaction Potentials of Anisotropic Nanocrystals from the Trajectory Sampling of Particle Motion Using *In Situ* Liquid Phase Transmission Electron Microscopy. *ACS Cent. Sci.* **2015**, *1*, 33−39.
(35) Tan, S. F.; Chee, S. W.; Lin, G.; Mirsaidov, U. Direct Observation of Interactions between Nanoparticles and Nanoparticle Self-Assembly in Solution. *Acc. Chem. Res.* **2017**, *50*, 1303−1312.
(36) Chen, Q.; Smith, J. M.; Park, J.; Kim, K.; Ho, D.; Rasool, H. I.; Zettl, A.; Alivisatos, A. P. 3D Motion of DNA-Au Nanoconjugates in Graphene Liquid Cell Electron Microscopy. *Nano Lett.* **2013**, *13*, 4556−4561.
(37) Canepa, S. A.; Sneed, B. T.; Sun, H.; Unocic, R. R.; Mølhave, K. Influence of Cetyltrimethylammonium Bromide on Gold Nanocrystal Formation Studied by *In Situ* Liquid Cell Scanning Transmission Electron Microscopy. *J. Phys. Chem. C* **2018**, *122*, 2350−2357.
(38) Robertson, A. W.; Zhu, G.; Mehdi, B. L.; Jacobs, R. M. J.; De Yoreo, J.; Browning, N. D. Nanoparticle Immobilization for Controllable Experiments in Liquid-Cell Transmission Electron Microscopy. *ACS Appl. Mater. Interfaces* **2018**, *10*, 22801−22808.
(39) Hauwiller, M. R.; Ondry, J. C.; Alivisatos, A. P. Using Graphene Liquid Cell Transmission Electron Microscopy to Study *In Situ* Nanocrystal Etching. *J. Visualized Exp.* **2018**, No. 135, 1−9.
(40) Ye, X.; Jones, M. R.; Frechette, L. B.; Chen, Q.; Powers, A. S.; Ercius, P.; Dunn, G.; Rotskoff, G. M.; Nguyen, S. C.; Adiga, V. P.; Zettl, A.; Rabani, E.; Geissler, P. L.; Alivisatos, A. P. Single-Particle Mapping of Nonequilibrium Nanocrystal Transformations. *Science* **2016**, *354*, 874−877.
(41) Hauwiller, M. R.; Ondry, J. C.; Chan, C. M.; Khandekar, P.; Yu, J.; Alivisatos, A. P. Gold Nanocrystal Etching as a Means of Probing the Dynamic Chemical Environment in Graphene Liquid Cell Electron Microscopy. *J. Am. Chem. Soc.* **2019**, *141*, 4428−4437.
(42) Hauwiller, M. R.; Frechette, L. B.; Jones, M. R.; Ondry, J. C.; Rotskoff, G. M.; Geissler, P.; Alivisatos, A. P. Unraveling Kinetically-Driven Mechanisms of Gold Nanocrystal Shape Transformations Using Graphene Liquid Cell Electron Microscopy. *Nano Lett.* **2018**, *18*, 5731−5737.
(43) Hu, X.; Cheng, W.; Wang, T.; Wang, E.; Dong, S. Well-Ordered End-To-End Linkage of Gold Nanorods. *Nanotechnology* **2005**, *16*, 2164−2169.
(44) Sudeep, P. K.; Joseph, S. T. S.; Thomas, K. G. Selective Detection of Cysteine and Glutathione Using Gold Nanorods. *J. Am. Chem. Soc.* **2005**, *127*, 6516−6517.

https://dx.doi.org/10.1021/acsnano.0c03601
ACS Nano 2020, 14, 10239−10250

(45) Nikoobakht, B.; El-Sayed, M. A. Preparation and Growth Mechanism of Gold Nanorods (NRs) Using Seed-Mediated Growth Method. *Chem. Mater.* **2003**, *15*, 1957−1962.
(46) O'Brien, M. N.; Jones, M. R.; Brown, K. A.; Mirkin, C. A. Universal Noble Metal Nanoparticle Seeds Realized through Iterative Reductive Growth and Oxidative Dissolution Reactions. *J. Am. Chem. Soc.* **2014**, *136*, 7603−7606.
(47) Nikoobakht, B.; El-Sayed, M. A. Evidence for Bilayer Assembly of Cationic Surfactants on the Surface of Gold Nanorods. *Langmuir* **2001**, *17*, 6368−6374.
(48) Gómez-Graña, S.; Hubert, F.; Testard, F.; Guerrero-Martínez, A.; Grillo, I.; Liz-Marzán, L. M.; Spalla, O. Surfactant (Bi)Layers on Gold Nanorods. *Langmuir* **2012**, *28*, 1453−1459.
(49) Jones, M. R.; Macfarlane, R. J.; Prigodich, A. E.; Patel, P. C.; Mirkin, C. A. Nanoparticle Shape Anisotropy Dictates the Collective Behavior of Surface-Bound Ligands. *J. Am. Chem. Soc.* **2011**, *133*, 18865−18869.
(50) Nie, Z.; Fava, D.; Rubinstein, M.; Kumacheva, E. Supramolecular" Assembly of Gold Nanorods End-Terminated with Polymer "Pom-Poms": Effect of Pom-Pom Structure on the Association Modes. *J. Am. Chem. Soc.* **2008**, *130*, 3683−3689.
(51) Hong, R.; Fischer, N. O.; Emrick, T.; Rotello, V. M. Surface PEGylation and Ligand Exchange Chemistry of FePt Nanoparticles for Biological Applications. *Chem. Mater.* **2005**, *17*, 4617−4621.
(52) Bajaj, A.; Miranda, O. R.; Kim, I.-B.; Phillips, R. L.; Jerry, D. J.; Bunz, U. H. F.; Rotello, V. M. Detection and Differentiation of Normal, Cancerous, and Metastatic Cells Using Nanoparticle-Polymer Sensor Arrays. *Proc. Natl. Acad. Sci. U. S. A.* **2009**, *106*, 10912−10916.
(53) Zeng, J.; Zheng, Y.; Rycenga, M.; Tao, J.; Li, Z. Y.; Zhang, Q.; Zhu, Y.; Xia, Y. Controlling the Shapes of Silver Nanocrystals with Different Capping Agents. *J. Am. Chem. Soc.* **2010**, *132*, 8552−8553.
(54) Vigderman, L.; Khanal, B. P.; Zubarev, E. R. Functional Gold Nanorods: Synthesis, Self-Assembly, and Sensing Applications. *Adv. Mater.* **2012**, *24*, 4811−4841.
(55) Zhang, H.; Hu, B.; Sun, L.; Hovden, R.; Wise, F. W.; Muller, D. A.; Robinson, R. D. Surfactant Ligand Removal and Rational Fabrication of Inorganically Connected Quantum Dots. *Nano Lett.* **2011**, *11*, 5356−5361.
(56) Chen, J.; Meng, Q.; May, P. S.; Berry, M. T.; Lin, C. Sensitization of Eu3+ Luminescence in Eu:YPO4 Nanocrystals. *J. Phys. Chem. C* **2013**, *117*, 5953−5962.
(57) Cross, A. M.; May, P. S.; Van Veggel, F. C. J. M.; Berry, M. T. Dipicolinate Sensitization of Europium Luminescence in Dispersible 5%Eu:LaF3 Nanoparticles. *J. Phys. Chem. C* **2010**, *114*, 14740−14747.
(58) Tan, S. F.; Anand, U.; Mirsaidov, U. Interactions and Attachment Pathways between Functionalized Gold Nanorods. *ACS Nano* **2017**, *11*, 1633−1640.
(59) Plateau, J. *Experimental and Theoretical Statics of Liquids Subject to Molecular Forces Only*; Gauthier-Villars: Paris, 1873, pp 1−427.
(60) Rayleigh, L. On The Instability Of Jets. *Proc. London Math. Soc.* **1878**, *s1−10*, 4−13.
(61) Nichols, F. A.; Mullins, W. W. Morphological Changes of a Surface of Revolution Due to Capillarity-Induced Surface Diffusion. *J. Appl. Phys.* **1965**, *36*, 1826−1835.
(62) Nichols, F. A.; Mullins, W. W. Surface- (Interface-) and Volume Diffusion Contributions to Morphological Changes Driven by Capillarity. *AIME Metall. Soc. Trans.* **1965**, *233*, 1840−1848.
(63) Toimil Molares, M. E.; Balogh, A. G.; Cornelius, T. W.; Neumann, R.; Trautmann, C. Fragmentation of Nanowires Driven by Rayleigh Instability. *Appl. Phys. Lett.* **2004**, *85*, 5337−5339.
(64) Novo, C.; Mulvaney, P. Charge-Induced Rayleigh Instabilities in Small Gold Rods. *Nano Lett.* **2007**, *7*, 520−524.
(65) Wang, T.; Hu, X.; Dong, S. The Fragmentation of Gold Nanoparticles Induced by Small Biomolecules. *Chem. Commun.* **2008**, No. 38, 4625.
(66) Xu, S.; Li, P.; Lu, Y. *In Situ* Atomic-Scale Analysis of Rayleigh Instability in Ultrathin Gold Nanowires. *Nano Res.* **2018**, *11*, 625−632.
(67) Bettscheider, S.; Kraus, T.; Fleck, N. A. On the Geometric Stability of an Inorganic Nanowire and an Organic Ligand Shell. *J. Mech. Phys. Solids* **2019**, *123*, 3−19.
(68) Alonso, C.; Salvarezza, R. C.; Vara, J. M.; Arvia, A. J. The Surface Diffusion of Gold Atoms on Gold Electrodes in Acid Solution and Its Dependence on the Presence of Foreign Adsorbates. *Electrochim. Acta* **1990**, *35*, 1331−1336.
(69) Ni, W.; Kou, X.; Yang, Z.; Wang, J. Tailoring Longitudinal Surface Plasmon Wavelengths, Scattering and Absorption Cross Sections of Gold Nanorods. *ACS Nano* **2008**, *2*, 677−686.
(70) Zou, R.; Guo, X.; Yang, J.; Li, D.; Peng, F.; Zhang, L.; Wang, H.; Yu, H. Selective Etching of Gold Nanorods by Ferric Chloride at Room Temperature. *CrystEngComm* **2009**, *11*, 2797.
(71) Abidi, W.; Selvakannan, P. R.; Guillet, Y.; Lampre, I.; Beaunier, P.; Pansu, B.; Palpant, B.; Remita, H. One-Pot Radiolytic Synthesis of Gold Nanorods and Their Optical Properties. *J. Phys. Chem. C* **2010**, *114*, 14794−14803.
(72) Joshi, S. S.; Patil, S. F.; Iyer, V.; Mahumuni, S. Radiation Induced Synthesis and Characterization of Copper Nanoparticles. *Nanostruct. Mater.* **1998**, *10*, 1135−1144.
(73) Fendler, J. H.; Bogan, G. W.; Fendler, E. J.; Infante, G. A.; Jirathana, P. Micellar Effects in Steady-State Radiation Induced Reactions. In *Reaction Kinetics in Micelles*; Springer US: Boston, MA, 1973; Vol. *53*, pp 53−71.
(74) Trifunac, A. D.; Nelson, D. J. Chemically Induced Dynamic Electron Polarization. Pulse Radiolysis of Aqueous Solutions of Micelles. *Chem. Phys. Lett.* **1977**, *46*, 346−348.
(75) Packer, J. E.; Winchester, R. V. Radiolysis of Neutral Aqueous Solutions of Cysteine in the Presence of Oxygen. *Chem. Commun.* **1968**, *1968*, 826−827.
(76) Garrison, W. M. Reaction Mechanisms in the Radiolysis of Peptides, Polypeptides, and Proteins. *Chem. Rev.* **1987**, *87*, 381−398.
(77) Faucitano, A.; Buttafava, A.; Martinotti, F.; Ferloni, P.; Magistris, A. The Mechanism of Gamma-Radiolysis of Polymethylene, Polypropylene and Poly-n-Butylene Oxides: An ESR Investigation. *Int. J. Radiat. Appl. Instrumentation. Part C. Radiat. Phys. Chem.* **1992**, *40*, 347−355.
(78) Zakurdaeva, O. A.; Nesterov, S. V.; Feldman, V. I. Radiolysis of Aqueous Solutions of Poly(Ethylene Oxide) at 77 K. *High Energy Chem.* **2005**, *39*, 201−206.
(79) Gröllmann, U.; Schnabel, W. On the Kinetics of Polymer Degradation in Solution, 9. Pulse Radiolysis of Poly(ethylene Oxide). *Makromol. Chem.* **1980**, *181*, 1215−1226.
(80) Schneider, N. M.; Norton, M. M.; Mendel, B. J.; Grogan, J. M.; Ross, F. M.; Bau, H. H. Electron-Water Interactions and Implications for Liquid Cell Electron Microscopy. *J. Phys. Chem. C* **2014**, *118*, 22373−22382.
(81) Charlesby, A.; Kopp, P. M. Radiation Protection of Aqueous Polyethylene Oxide Solutions by Thiourea. *Proc. R. Soc. London, Ser. A* **1966**, *291*, 129−143.
(82) Grogan, J. M.; Schneider, N. M.; Ross, F. M.; Bau, H. H. Bubble and Pattern Formation in Liquid Induced by an Electron Beam. *Nano Lett.* **2014**, *14*, 359−364.
(83) Cho, H.; Jones, M. R.; Nguyen, S. C.; Hauwiller, M. R.; Zettl, A.; Alivisatos, A. P. The Use of Graphene and Its Derivatives for Liquid-Phase Transmission Electron Microscopy of Radiation-Sensitive Specimens. *Nano Lett.* **2017**, *17*, 414−420.
(84) Baumgardner, W. J.; Whitham, K.; Hanrath, T. Confined-But-Connected Quantum Solids *via* Controlled Ligand Displacement. *Nano Lett.* **2013**, *13*, 3225−3231.
(85) Sandeep, C. S. S.; Azpiroz, J. M.; Evers, W. H.; Boehme, S. C.; Moreels, I.; Kinge, S.; Siebbeles, L. D. A.; Infante, I.; Houtepen, A. J. Epitaxially Connected PbSe Quantum-Dot Films: Controlled Neck Formation and Optoelectronic Properties. *ACS Nano* **2014**, *8*, 11499−11511.
(86) Phan, H. T.; Haes, A. J. What Does Nanoparticle Stability Mean? *J. Phys. Chem. C* **2019**, *123*, 16495.

https://dx.doi.org/10.1021/acsnano.0c03601
ACS Nano 2020, 14, 10239−10250

(87) Hufschmid, R.; Teeman, E.; Mehdi, B. L.; Krishnan, K. M.; Browning, N. D. Observing the Colloidal Stability of Iron Oxide Nanoparticles *In Situ*. *Nanoscale* **2019**, *11*, 13098−13107.
(88) Ye, X.; Zheng, C.; Chen, J.; Gao, Y.; Murray, C. B. Using Binary Surfactant Mixtures To Simultaneously Improve the Dimensional Tunability and Monodispersity in the Seeded Growth of Gold Nanorods. *Nano Lett.* **2013**, *13*, 765−771.

https://dx.doi.org/10.1021/acsnano.0c03601
ACS Nano 2020, 14, 10239−10250